Pressure-induced polymorphism in hypervalent CsI_3

Nishant N. Patel, Meenakshi Sunder,* Alka B. Garg, and H. K. Poswal
High Pressure & Synchrotron Radiation Physics Division, Bhabha Atomic Research Centre, Trombay-400 085, India
(Received 20 July 2017; revised manuscript received 2 November 2017; published 27 November 2017)

We report the results of ambient temperature high-pressure synchrotron-based x-ray diffraction, Raman, and electrical resistance study of CsI_3 up to 29, 25, and 8 GPa, respectively, and confirm three-phase transitions under quasihydrostatic conditions. The ambient orthorhombic (space group (SG): *Pnma*) phase of CsI_3 is stable up to a pressure of ∼1.3 GPa, above which a phase transition to a trigonal (SG : P-3c1) phase is observed. The stability region of the trigonal phase has been found to be up to 22.6 GPa, above which the trigonal phase transforms to a cubic (SG : Pm-3n) phase which remains stable until the maximum pressure of 29 GPa achieved in this study. A third-order Birch-Murnaghan equation of state fit to the pressure volume (P-V) data yields a bulk modulus of 17.7(9) GPa for the trigonal phase. Raman spectroscopic measurements however indicate three-phase transitions at ∼1.3, 4.0, and 22.6 GPa, respectively. The electrical resistance measured in the low-pressure region up to 8 GPa indicates an electronic transition at around 4 GPa confirming the Raman result observed at 4.0 GPa. The P-V data when transformed to the universal equation of state (UEOS) show a deviation from linearity around 4.0 GPa confirming the electronic transition. The present study has thus revealed a three-phase structural sequence in alkali trihalides, *viz.,* orthorhombic (SG: *Pnma*) to trigonal (SG : P-3c1) to a cubic (SG : Pm-3n) phase.

DOI: 10.1103/PhysRevB.96.174114

I. INTRODUCTION

The alkali halides serve as the simplest and model ionic solid for both static and dynamic high-pressure investigations. They exhibit a wide variety of phenomena like structural phase transition, metallization, superconductivity, etc., when subjected to compression, and hence have been extensively investigated both experimentally and theoretically for their high-pressure behavior [1–6]. Interest in the alkali halide system has been rekindled by the recent studies which have reported the formation of low-symmetry new unconventional stoichiometric compounds with unusual bonding and electronic properties like $NaCl_3$, Na_3Cl, KCl_3, KBr_3, KBr_5, etc., by combining theoretical predictions and diamond-anvil-cell-based high-pressure experiments [7–9]. $NaCl_3$ at high temperature and high pressure is reported to be stable between 20 and 48 GPa and has a *Pnma* structure; at 48 GPa it reportedly undergoes a phase transformation into a metallic *Pm-3n* phase and decomposes to NaCl and Cl_2 below 18 GPa on pressure release. In the K-Br system, KBr_3 formed in a chemical reaction between KBr and Br_2 above 2 GPa at room temperature has been reported to crystallize in the primitive orthorhombic structure (SG: *Pnma*). On further compression a monoclinic KBr_5 (SG: $P2_1$) has been reported at ∼6.0 GPa which decomposes to a trigonal (SG: P-3c1) KBr_3 and Br_2 above 14 GPa and 1500 K [9].

Interestingly, among the alkali halides the cesium iodide solution is able to dissolve iodine, bromine, or chlorine, and produce crystals whose chemical analysis could be expressed by the empirical formulas CsI_3, $CsIBr_2$, $CsBrI_2$, $CsICl_2$, CsIBrCl, etc. [10]. Furthermore CsI_3 and $CsIBr_2$ have been known to adopt an orthorhombic (SG: *Pnma*) structure under ambient conditions, which is the same structure as the alkali trihalides observed in the Na-Cl and K-Br systems [7,9]. It may also be noted that $NaCl_3$ is stabilized both in the orthorhombic (SG: *Pnma)* and cubic (SG : Pm-3n) phase in the Na-Cl system, whereas KCl_3 is stabilized both in the trigonal (SG : P-3c1) and cubic (SG : Pm-3n) phase in the K-Cl system and KBr_3 is stabilized both in the orthorhombic (SG: *Pnma)* and trigonal (SG : P-3c1) phase in the K-Br system. Table I summarizes the pressure range of phase stability of the various alkali trihalides. The absence of trigonal phase in $NaCl_3$, orthorhombic phase in KCl_3, and cubic phase in KBr_3 makes it difficult to arrive at a systematics for the high-pressure structural transition sequence in alkali trihalide systems. Very recently, theoretical calculations by Wei *et al.* have predicted a *Pm-3n* phase for CsI_3 under high pressure wherein endless linear chain-type structure, due to the hypervalence phenomenon of iodine, is reported [11]. Furthermore, their calculations have also revealed a metallic phase for the *Pm-3n* phase of CsI_3. In light of the above discussion, experimental high-pressure investigations on CsI_3 could shed more light on understanding its structural evolution and give better insight into the search for alkali polyhalides.

With this motivation we have carried out high-pressure structural, vibrational, and electrical transport investigations on CsI_3 at high pressure and room temperature. Existence of high-purity stable single-phase CsI_3 at ambient condition justifies our preference of CsI_3 over other trihalides. In addition, the recent prediction of superconductivity at very low pressure ∼10 GPa in the predicted cubic phase of CsI_3 has further encouraged us to investigate the high-pressure behavior of CsI_3 [11].

To the best of our knowledge there are no experimental reports of high-pressure investigations on CsI_3. In the present study the high-pressure behavior of CsI_3 at ambient temperature has been investigated through synchrotron-based angle-dispersive x-ray diffraction (ADXRD) up to 29 GPa, Raman spectroscopy up to 25 GPa, and Bridgman anvil apparatus-based electrical resistance measurements up to 8 GPa to look for the possibility of structural or electronic transition and any possible metallization under compression.

*msunder@barc.gov.in

TABLE I. Pressure range of stability of the various alkali trihalides.

Material	Pressure range of stability		
	Orthorhombic (SG: *Pnma*) phase (GPa)	Trigonal (SG : P-3c1) phase (GPa)	Cubic (SG : Pm-3n) phase (GPa)
$NaCl_3$ [7]	20–48		<48
KCl_3 [8]		8–20	<20
KBr_3 [9]	1–6	14–20	

We have confirmed three-phase transitions in CsI_3 up to 29 GPa under quasihydrostatic conditions. The structural study using ADXRD has revealed an orthorhombic (SG: *Pnma*) to trigonal (SG : P-3c1) phase transition above 1.3 GPa. The stability region of the trigonal phase was found to be up to 22.6 GPa. Above this pressure the trigonal phase was found to transform to a cubic (SG : Pm-3n) phase, which remained stable until the maximum pressure of 29 GPa achieved in this study. The structural details of the various phases have been obtained by Rietveld refinement. Raman spectroscopic measurements which verify the ADXRD results are also presented. The electrical resistance measured in the low-pressure region up to 8 GPa indicates an electronic transition at around 4 GPa which is well corroborated by the Raman and ADXRD results.

II. STRUCTURAL DETAILS

The structure of CsI_3 consists of Cs^+ and $[I_3]^-$ ions [12–14]. The I_3^- anion belongs to the class of hypervalent compounds which violate the Lewis octet rule [15,16]. It has a linear geometric structure where the central iodine atom shares two electrons with two adjacent iodine atoms by forming a three-center four-electron (3c-4e) bond and it gets one electron from cesium atom to keep the other two iodine atoms together [17]. In terms of the molecular orbitals the 3c-4e bond as indicated in Fig. 1(a) can be described by a set of three molecular orbitals (MOs) derived from colinear p orbitals on each iodine atom, and the two lower-energy MOs (bonding and nonbonding) are occupied by two electrons each. The structure of CsI_3 was proposed to be based on the simple orthorhombic lattice with space group *Pnma* as shown in Fig. 1(b) [18,19]. Interestingly, similar crystal structures with space group *Pnma* have been reported for $NaCl_3$ and KBr_3 under nonambient pressure and temperature conditions [7,9].

III. EXPERIMENTAL METHOD

A. Sample characterization

The polycrystalline CsI_3 of purity (99.9%) was procured commercially from Sigma-Aldrich. The sample was

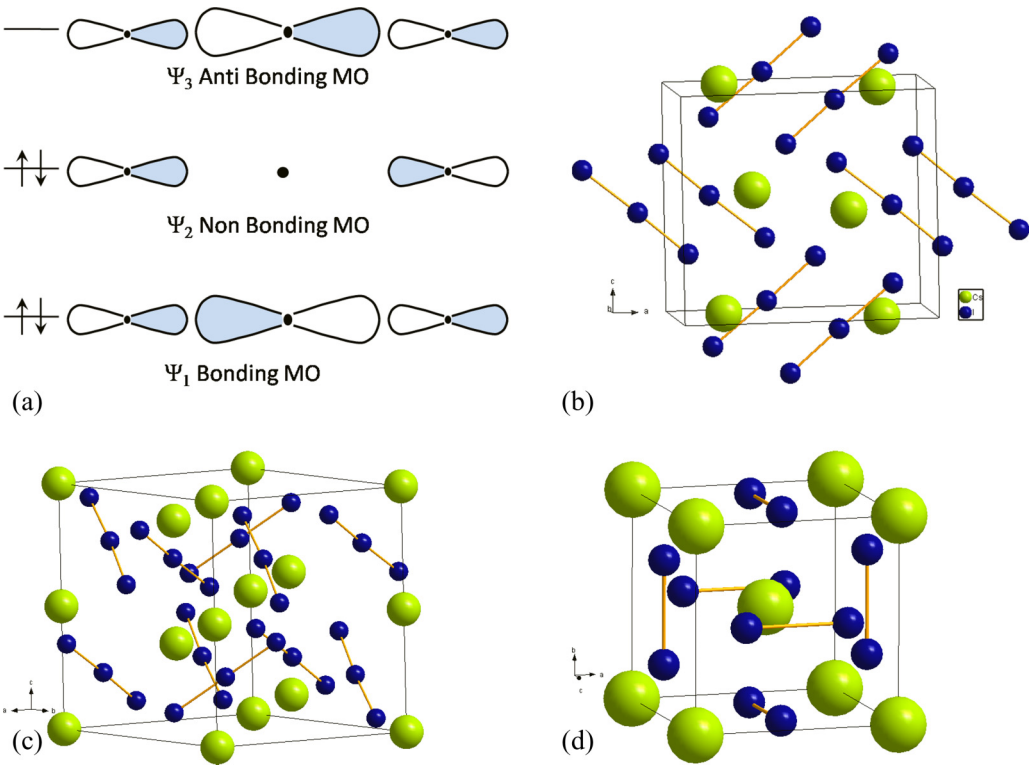

FIG. 1. (a) Molecular orbital representation of 3c-4e bond in I_3^-. Crystal structure of (b) orthorhombic (SG: *Pnma*), (c) trigonal (SG : P-3c1), and (d) cubic (SG : Pm-3n) CsI_3.

characterized using powder x-ray diffraction. The cell constants and atomic coordinates obtained by Rietveld refinement of the x-ray powder diffraction data confirmed it to be an orthorhombic (SG: *Pnma*, $Z = 4$) structure with lattice parameters [$a = 11.0837(7)$Å, $b = 6.8443(3)$Å, $c = 10.0262(6)$Å] in good agreement with the literature values [18,19]. The observed Raman spectrum at ambient conditions was consistent with the spectra reported earlier in the literature and the Raman frequencies were found to match well with the reported values [20].

B. X-ray diffraction

High-pressure ADXRD measurements were performed on powdered CsI_3 at room temperature up to 29 GPa on the Xpress beamline at the Elettra synchrotron radiation source, Trieste, Italy [21]. A modified Mao-Bell-type diamond-anvil cell (DAC) with diamonds of culet size 400 μm was used with ruby as the internal pressure calibrant. Silicone oil was used as the pressure-transmitting medium. It may be noted that a 4:1 methanol-ethanol mixture as well as glycerol were tried as the pressure medium. However, the sample was found to dissolve in these two media, which led us to select silicone oil as the pressure-transmitting medium. The sample chamber was a 150-μm-diameter hole drilled in a tungsten gasket of starting thickness 250 μm which was preindented to a thickness of 50 μm. Pressure measurements inside the sample chamber were carried out using an online ruby fluorescence setup installed at the Xpress beamline [21]. ADXRD diffraction patterns were collected using an image plate area detector (MarResearch) employing an x-ray wavelength of 0.5007 Å/0.4957 Å. The x-ray beam size was constrained using a circular pin hole of 30 μm diameter which eliminated the diffraction lines from the gasket. The sample to image plate distance was calibrated using LaB_6 and CeO_2 as standards. The x-ray data were collected at various pressures with a typical exposure time of about 10 min. The scanned two-dimensional diffraction images were corrected for image plate tilt and converted to intensity versus 2θ profile through radial integration using FIT2D software [22]. The lattice parameters of the sample were determined by carrying out full-profile Rietveld refinement using GSAS [23]. The parameters refined included the overall scaling factor, Chebyshev polynomial background, lattice constants, pseudo-Voigt profile function parameters, atomic fractional coordinates, and spherical harmonics correction. Multiphase refinement was carried out and the profile was fitted with the pseudo-Voigt peak shape with the background fitted by linear interpolation of selected set of points. The fitting procedure was iterative and was terminated on attaining an acceptable small weighted R factor or goodness of fit.

C. Raman measurements

High-pressure Raman investigations up to 25 GPa were carried out on polycrystalline CsI_3 using a modified Mao-Bell-type DAC and a micro-Raman system having a resolution of better than 2 cm^{-1} using a backscattering geometry. Raman signal excited using a 532-nm diode-pumped solid-state (DPSS) laser (Ventus, Laser Quantum) was collected using a Jobin Yvon T64000 triple-stage Raman spectrograph (with 1800 line grating) equipped with a Peltier cooled charge-coupled device detector (Synapse). The sample sensitivity to laser intensity was checked by collecting the ambient Raman spectra at various laser powers as shown in Fig. 2, which clearly indicate that the sample remains unaffected by the laser power in the present measurements. The sample loading procedure for these measurements was similar to the one described above for the XRD measurements. Silicone oil was used as the pressure-transmitting medium and pressure calibration was carried out using the ruby fluorescence technique. The Raman spectra for CsI_3 were recorded at different pressures under quasihydrostatic conditions in the entire spectral region of interest (50–250 cm^{-1}). The typical laser power and data collection time for the Raman measurements was 4 mW and 10 s, respectively.

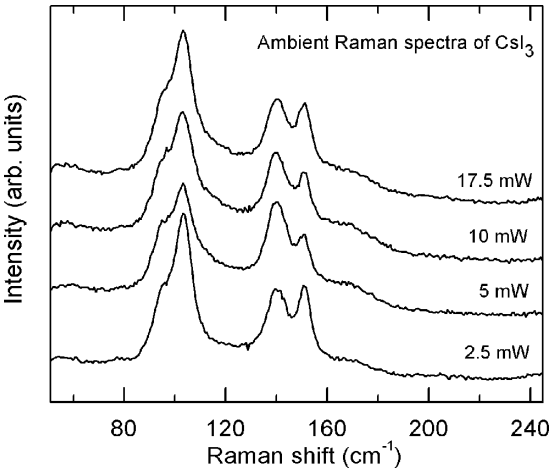

FIG. 2. Ambient Raman spectra of CsI_3 at various laser powers of the DPSS laser ($\lambda = 532$ nm).

D. Electrical resistance measurements

Electrical resistance measurements under pressure up to 8 GPa were carried out using an opposed Bridgman anvil setup consisting of a 12-mm-face-diameter tungsten carbide anvil pair [24]. A pair of pyrophyllite gasket of thickness 200 μm each with a central hole of 3 mm in diameter was used to contain the sample. Bismuth was used for the pressure calibration along with steatite as a pressure-transmitting medium. A well-compacted powdered sample of 2 mm × 1.5 mm × 0.1 mm in dimension was used for the four-probe electrical resistance measurements. A constant current was passed through the two outer leads by a Keithley source meter and voltage drop across the inner two leads was measured using a Keithley nanovoltmeter at each value of pressure with 2 min of pressure soaking time.

IV. RESULTS AND DISCUSSION

A. High-pressure x-ray diffraction

The evolution of diffraction patterns of CsI_3 during pressure increase is depicted in Fig. 3. The x-ray patterns could be indexed to the ambient orthorhombic (SG: *Pnma*) phase up to

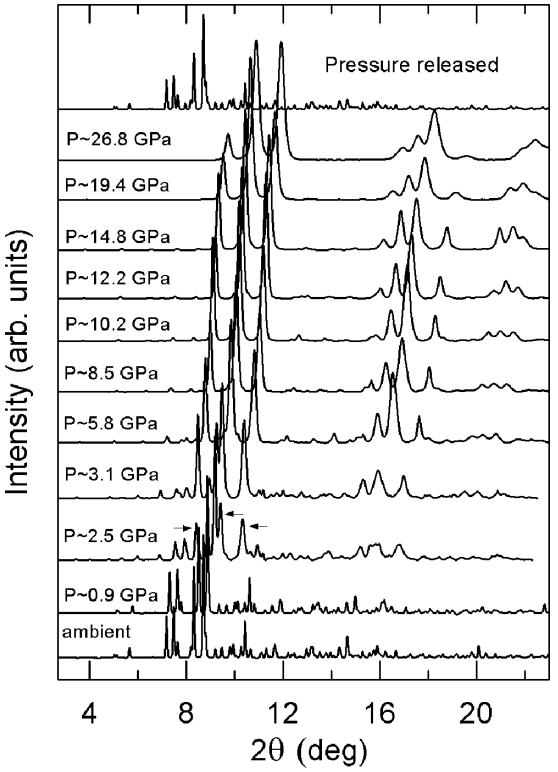

FIG. 3. Structural evolution of ADXRD pattern of CsI_3 with pressure. The arrows indicate the new peaks.

1.3 GPa. On further increase of pressure, additional diffraction peaks are seen to emerge along with those of the ambient orthorhombic phase indicating the onset of a structural phase transition above 1.3 GPa. As the pressure is further increased, the intensity of the diffraction peaks corresponding to the *Pnma* phase reduces and the intensity of the new peaks is seen to build up. The emerging diffraction peaks could be assigned to a trigonal (SG : P-3c1) phase by employing CRYSFIRE and CHECK CELL software [25–27]. The ambient and the trigonal

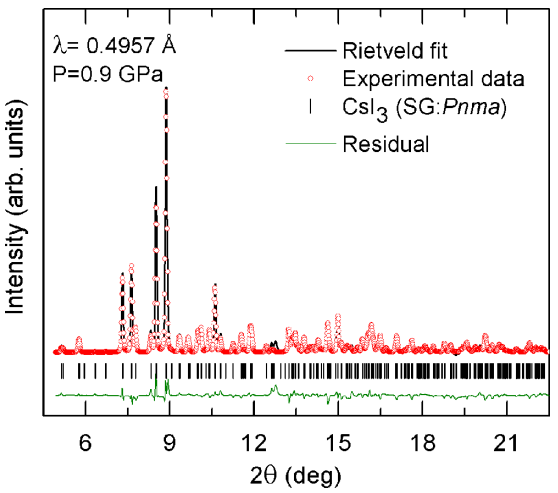

FIG. 4. Rietveld-refined ADXRD pattern of orthorhombic (SG: *Pnma*) CsI_3 at 0.9 GPa. The *Rp* and *wRp* factors of the fit are 3.8 and 5.9%, respectively.

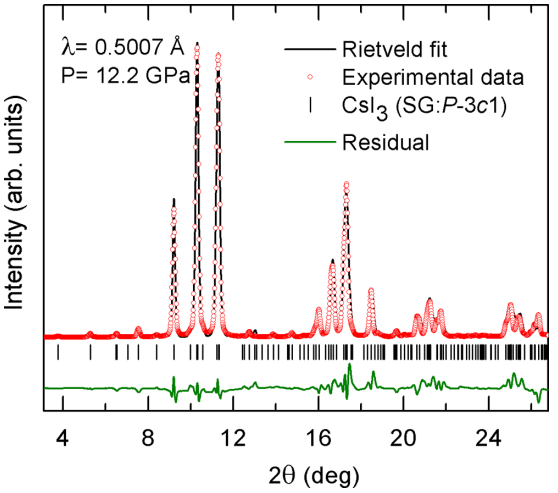

FIG. 5. Rietveld-refined ADXRD pattern of trigonal (SG: P-3c1) CsI_3 at 12.2 GPa. The *Rp* and *wRp* factors of the fit are 3.4 and 5.1%, respectively.

phase are seen to coexist up to a pressure of about 10 GPa. Interestingly, this trigonal structure is similar to the structure of KBr_3 and KCl_3 [8,9]. On further pressurization, CsI_3 is found to remain in the trigonal phase until 22.6 GPa. Beyond this pressure, the diffraction peaks associated with the trigonal phase with Miller indices (100), (002), (10-2), (110), (111), (200), (112), etc., are seen to disappear. The disappearance of these diffraction peaks indicates yet another structural phase transition. This high pressure phase could be indexed to a cubic (SG : Pm-3n) structure and it remains stable up to the highest pressure of 29 GPa achieved in the present study.

The multiphase Rietveld refinement of all the diffraction patterns was carried out to extract information on the structural evolution using GSAS software. A representative Rietveld refinement pattern for the ambient orthorhombic (SG: *Pnma*) phase collected at 0.9 GPa is shown in Fig. 4. The Rietveld-refined patterns of the trigonal and cubic phase are depicted in Figs. 5 and 6, respectively. The unit-cell parameters and

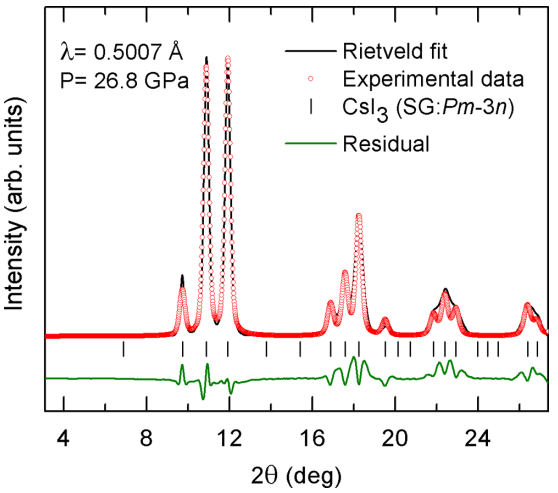

FIG. 6. Rietveld-refined ADXRD pattern of cubic (SG : Pm-3n) CsI_3 at 26.8 GPa. The *Rp* and *wRp* factors of the fit are 2.8 and 3.9%, respectively.

TABLE II. Unit-cell parameters and atomic coordinates of CsI_3 in the orthorhombic, trigonal, and cubic phase.

CsI_3 phase	Pressure (GPa)	Unit-cell parameters		Atomic coordinates		
		Lattice parameter (Å)	γ			$x\ y\ z$
Orthorhombic	0.9	$a = 10.9148(6)$	90°	Cs	$4c$	0.8320(5); 0.2500; 0.4672(5)
(SG : *Pnma*)		$b = 6.6755(3)$		I1	$4c$	0.5732(6); 0.2500; 0.7393(6)
		$c = 9.8240(5)$		I2	$4c$	0.3804(5); 0.2500; 0.5455(6)
				I3	$4c$	0.1636(6); 0.2500; 0.3535(5)
Trigonal	12.2	$a = 8.7896(4)$	120°	Cs1	$2b$	0.0000; 0.0000; 0.0000
(SG : P-3c1)		$c = 10.8780(8)$		Cs2	$4d$	0.3333; 0.6666; 0.8304(14)
				I1	$6f$	0.2405(12); 0.0000; 0.2500
				I2	$12g$	0.3488(6); 0.4294(8); 0.0699(5)
Cubic	26.8	$a = 5.9046(3)$	90°	Cs	$2a$	0.0000; 0.0000; 0.0000
(SG : Pm-3n)				I	$6c$	0.2500; 0.0000; 0.5000

the atomic coordinates extracted for the different phases are tabulated in Table II. Figures 1(c) and 1(d) show the crystal structure of CsI_3 in the trigonal (SG : P-3c1) and cubic (SG : Pm-3n) phase respectively. During decompression the cubic-to-trigonal transition is found to be reversible whereas the ADXRD pattern of the pressure-released sample, as shown in Fig. 7, indicates the coexistence of the trigonal and ambient orthorhombic phase. The variation of volume per formula unit as a function of pressure for the orthorhombic, trigonal, and cubic phase is shown in Fig. 8. It may be noted that the volume at ambient pressure (V_o) employed for the trigonal phase was obtained by extrapolating the P-V data to ambient pressure. The bulk modulus and its pressure derivative for the orthorhombic (SG: *Pnma*) and trigonal (SG : P-3c1) phases were calculated by a third-order Birch-Murnaghan equation of state [28] fit to the P-V data represented by

$$P(V) = (3/2)B_o[(V_o/V)^{7/3} - (V_o/V)^{5/3}] \times \{1 + 3/4(B' - 4)[(V_o/V)^{2/3} - 1]\}, \quad (1)$$

where B_o and V_o are the ambient pressure bulk modulus and volume, respectively, B' is the pressure derivative of bulk modulus, and V is the volume at pressure P. The results of the P-V data fitting are tabulated and compared with the analogous compound reported in the K-Br system in Table III. The bulk modulus for the cubic phase could not be determined because of fewer experimental data points. Pressure dependencies of the normalized lattice parameters for the orthorhombic (SG: *Pnma*) and trigonal (SG : P-3c1) phases are plotted in Figs. 9 and 10, respectively. The fitted linear moduli and their pressure derivatives are summarized in Table IV. It is evident from Table IV that in the orthorhombic phase, the largest unit-cell axis (a axis) is the least compressible, whereas the smallest unit-cell axis (b axis) is the most compressible. The layered structure along the b axis explains the high compressibility in this direction and resultant low linear modulus for the b axis, whereas the presence of a large number of sigma bonds in the ac plane explains the low compressibility of the a- and c

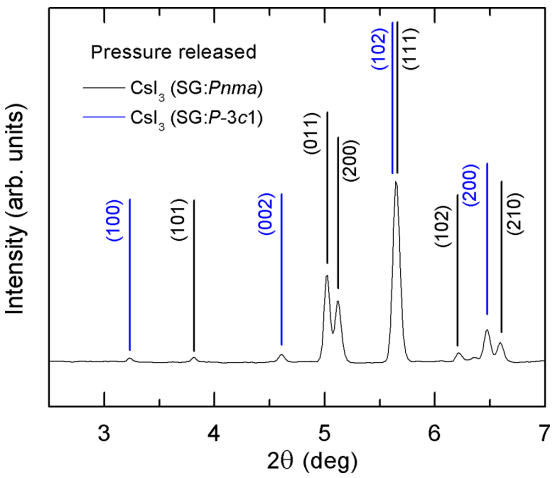

FIG. 7. ADXRD pattern in the 2θ range of 2° to 7° for pressure-released CsI_3 depicting the coexistence of orthorhombic and trigonal phases at ambient condition.

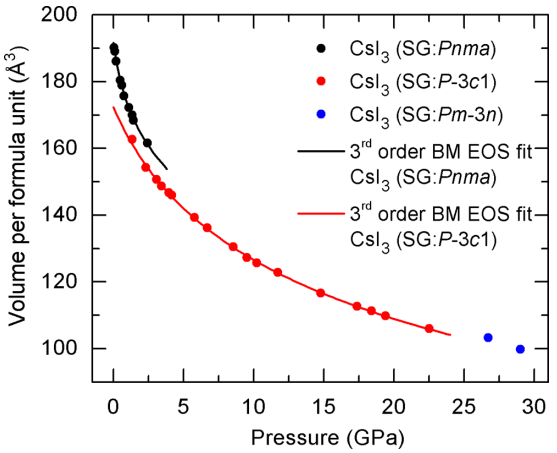

FIG. 8. Variation of volume per formula unit as a function of pressure for all the three phases (orthorhombic, trigonal, and cubic) of CsI_3. Symbols denote the experimental data points and solid lines denote third-order Birch-Murnaghan equation of state fit to the data. Error bars are within symbols.

TABLE III. Unit-cell volume (V_0 in Å^3), bulk modulus (B_o in GPa), and pressure derivative of bulk modulus (B') obtained by fitting the third-order Birch-Murnaghan equation of state to the P-V data of orthorhombic and trigonal CsI_3. The corresponding data for KBr_3 [9] are also tabulated for comparison.

	CsI_3		KBr_3 [9]	
	Pnma	*P*-3*c*1	*Pnma*	*P*-3*c*1
V_0(Å^3)	766.4(16)	1034(6)	534.37	770.73
Bulk modulus B_0 (GPa)	5.6(6)	17.7(9)	11.8	15.5
B'	12(2)	3.94(12)	4.0	4.55

axes. In the trigonal phase, the c axis is seen to be little more compressible than the a- and b axes.

B. High-pressure Raman spectroscopy

Figure 11 shows the evolution of Raman spectra of CsI_3 with pressure. The Raman spectra of CsI_3 at ambient condition as depicted in Fig. 11 are in good agreement with the reported values [20]. There are five distinct Raman modes observed at 94, 102, 138.7, 149, and 167.5 cm^{-1} at ambient condition. The Raman modes at 94 and 102 cm^{-1} could be attributed to the symmetrical stretching vibration of the I_3^- units. The Raman modes at 138.7 and 149 cm^{-1} correspond to the antisymmetrical stretching vibration of the I_3^- units. With increasing pressure, all the Raman-mode frequencies show a positive slope with pressure. Above 1.3 GPa abrupt changes in the Raman spectra are observed and additional Raman modes appear at 59.0, 77.0, and 110.3 cm^{-1}. The appearance of these Raman modes above 1.3 GPa indicates the onset of a phase transition. This high pressure phase has been attributed to the trigonal *(SG : P-3c1)* phase as observed in our present ADXRD measurements. On further increase of pressure, the highest-frequency Raman mode corresponding to the *Pnma* phase is seen to survive up to 10 GPa along with the Raman modes corresponding to the trigonal phase,

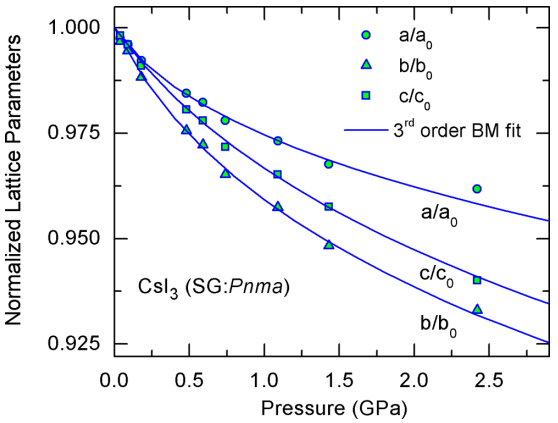

FIG. 9. Variation of normalized lattice parameters of CsI_3 in the orthorhombic (SG: *Pnma*) phase with pressure. The symbols and solid line denote the experimental data points and the third-order Birch-Murnaghan equation of state fit to the experimental data, respectively. Error bars are within symbols.

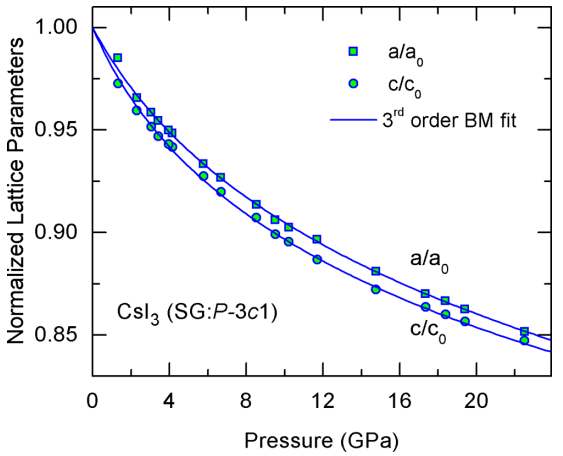

FIG. 10. Variation of normalized lattice parameters of CsI_3 in the trigonal (SG : *P*-3*c*1) phase with pressure. The symbols and solid line denote the experimental data points and the third-order Birch-Murnaghan equation of state fit to the experimental data, respectively. Error bars are within symbols.

confirming coexistence of both the phases in the pressure range of 1.3 to 10 GPa. The pressure dependence of mode frequencies is shown in Fig. 12. Raman-mode frequencies at ambient pressure and coefficient of their pressure derivatives obtained by linear or quadratic fit are summarized in Table V. Above 4.0 GPa a splitting is observed for the Raman mode at 107 and 118 cm^{-1}. In addition, major intensity redistribution is observed in the overall Raman spectra. It is evident from Fig. 12 that all the Raman modes show a change of slope above 4.0 GPa. Hence the various attributes around 4.0 GPa such as slope change and mode splitting indicate yet another phase transition in CsI_3. At still higher pressures the intensities of all the Raman modes are found to decrease with increasing pressure. Above 13 GPa the mode at 77 cm^{-1} is found to soften and a complete loss of Raman intensity is observed above 22.6 GPa, indicating a phase transformation to a Raman inactive phase or amorphization or band-gap closure/collapse. However, based on our ADXRD measurements this transition has been attributed to the structural phase transition to the cubic

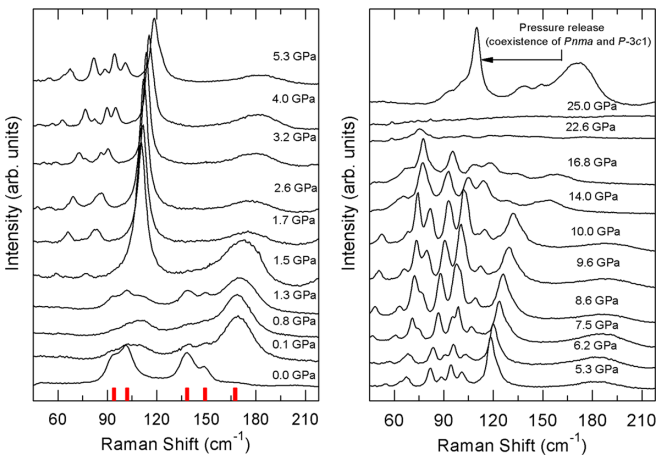

FIG. 11. Pressure evolution of Raman spectra of CsI_3. The bars indicate the Raman modes at ambient conditions.

TABLE IV. Unit-cell parameters (a_0,b_0,c_0 in Å), linear modulus (M_0 in GPa), and pressure derivative of linear modulus (M') at ambient pressure obtained by fitting the third-order Birch-Murnaghan equation of state to the pressure variation of lattice parameters of orthorhombic and trigonal CsI_3.

CsI_3	a_0 (Å)	M_{0a} (GPa)	M_a'	b_0 (Å)	M_{0b} (GPa)	M_b'	c_0 (Å)	M_{0c} (GPa)	M_c'
Pnma	11.111(14)	18(6)	77(36)	6.866(6)	13.7(15)	29(5)	10.045(7)	19.9(17)	24(4)
P-3*c*1	9.846(16)	57(3)	11.4(3)	9.846(16)	57(3)	11.4(3)	12.32(6)	45(6)	12.8(10)

(SG : *Pm*-3*n)* phase. It may be noted that this cubic phase in CsI_3 has been reported to be a metallic phase by theoretical calculation by Wei *et al.* [11]. Similar crystal structure has also been reported for $NaCl_3$ [7]. Reappearance of Raman modes during pressure release reconfirms the reversible nature of the observed phase transition. The pressure-released pattern shows Raman modes of both trigonal and ambient orthorhombic phase corroborating our ADXRD results. The existence of the trigonal phase upon pressure release suggests a small energy difference between the trigonal and the orthorhombic phase.

C. High-pressure electrical resistance measurements

Figure 13 depicts the variation of electrical resistance with pressure for CsI_3. Initially the resistance decreases with pressure up to 1.6 GPa and beyond this pressure it starts increasing. This change in the slope is attributed to the orthorhombic-to-trigonal phase transition observed in the XRD and Raman measurements. On further increase of pressure, the resistance continues to increase with a plateaulike region up to 4.5 GPa, beyond which there is an exponential increase in the resistance, and around 8 GPa the resistance value exceeds the limit of the measuring instrument. This sharp increase in the resistance, in the absence of any structural phase transition as observed in our XRD studies, is indicative of major electronic rearrangements. The changes observed in the Raman spectra around 4.0 GPa also corroborate the present observation. It is also noteworthy that a reversible behavior is observed on pressure release consistent with our Raman and ADXRD measurements.

A significant feature of the present study is the observation of a transition around 1.3 GPa in the x-ray measurements which is well corroborated by Raman and electrical resistance measurements. Hence we attribute this to a first-order structural transition from an orthorhombic (SG: *Pnma*) to a trigonal (SG : *P*-3*c*1) phase accompanied with volume discontinuity of 4.5%. It may also be noted that although Raman spectra show significant changes around 4.0 GPa, our x-ray diffraction measurements indicate no signature of any structural phase transition around this pressure (Supplemental Material, Fig. S1) [29]. Furthermore, an anomaly is also observed in the electrical resistance measurements. The *P*-*V* data as shown in Fig. 8 do not reveal any discontinuity around 4.0 GPa. This leads us to believe that this transition could be an electronic transition.

In order to better understand the anomaly in the Raman and resistance data we have analyzed the experimental *P*-*V* data for the trigonal phase through the use of the universal equation of state (UEOS) calculated by fixing V_o to the extrapolated value at ambient pressure [30]. The universal EOS can be represented as follows:

$$\ln H = \ln[PX^2/3(1-X)] = \ln B_0 + \eta(1-X), \qquad (2)$$

where $X = (V/V_o)^{1/3}$, P is the pressure, V_o is the ambient volume, and η is related to B_o' by

$$\eta = 3(B_o' - 1)/2.$$

In particular, electronic transition will lead to a deviation from linearity in the universal equation of state [30,31]. As observed from the UEOS plot shown in Fig. 14, there is indeed

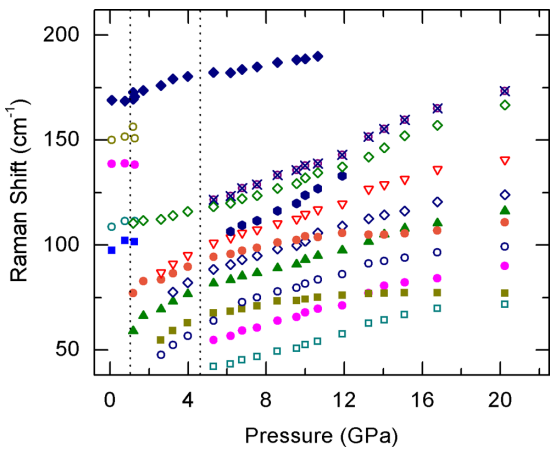

FIG. 12. Variation of Raman mode frequencies of CsI_3 with pressure. Dotted vertical lines are placed at the phase transition boundary. Error bars are within symbols.

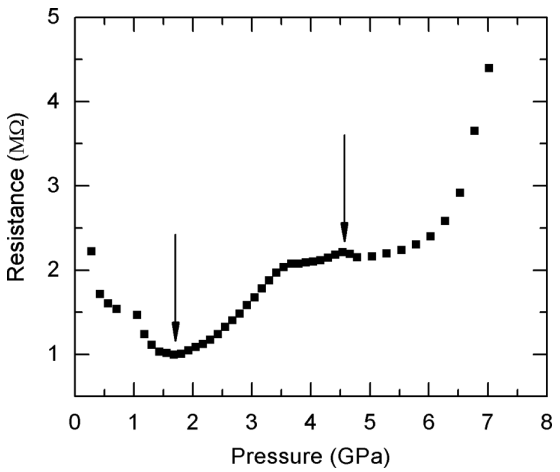

FIG. 13. Variation of electrical resistance of CsI_3 with pressure. Arrows denote the transition points.

TABLE V. Raman-mode frequencies of CsI_3 at ambient pressure (ω_0) and their pressure coefficients for the orthorhombic and trigonal phase obtained by a linear or quadratic fit.

Orthorhombic (SG: *Pnma*) phase in the pressure range of 0.1 MPa to 1.3 GPa		Trigonal (SG : *P*-3*c*1) phase in the pressure range of 1.3 to 4.0 GPa		Trigonal (SG : *P*-3*c*1) phase in the pressure range of 4.0 to 20 GPa		
ω (cm^{-1}) at 0.1 MPa	$d\omega_0/dp$ (cm^{-1}/GPa)	ω (cm^{-1}) at 2.6 GPa	$d\omega_0/dp$ (cm^{-1}/GPa)	ω (cm^{-1}) at 5.3 GPa	$d\omega_0/dp$ (cm^{-1}/GPa)	$d^2\omega_0/dp^2$ (cm^{-1}/GPa^2)
94	3.7(24)	47.7	6.5(5)	42	2.3(1)	
102	2.5(12)	54.7	5.8(7)	54.6	2.5(1)	
138.7	−0.3(4)	69.3	5.9(8)	63.8	5.5(4)	−0.12(1)
149	0.7(12)	73.2	6.1	67.5	2.7(1)	−0.081(6)
167.5	1.9(1)	83.5	4.0(7)	81.8	2.5(1)	
		86.9	5.9(5)	88.4	2.6(1)	
		112.2	1.9(3)	94.3	3.8(4)	−0.12(2)
				101.0	2.9(1)	
				104.4	4.6(2)	
				118.2	3.4(1)	
				121.7	3.7(1)	

a change of slope corresponding to a pressure of ∼4.1 GPa [$(1 - X) \sim 0.06$]. This pressure is in good agreement with the pressure at which the Raman modes show splitting and is also consistent with the anomaly observed between 4 and 5 GPa in the electrical resistance behavior with pressure. This leads us to conclude that CsI_3 shows an electronic transition at ∼4.0 GPa.

It is worth noting that up to now all the alkali trihalide high-pressure phases ($NaCl_3$, KBr_3, KCl_3) have been reported to decompose on pressure release to ambient conditions [7–9]. The recovery of CsI_3 in the metastable high-pressure phase (SG : *P*-3*c*1) at ambient conditions thus makes CsI_3 unique in the whole alkali polyhalogen system reported so far. This may have considerable impact on the ongoing search and synthesis of alkali polyhydrides which are also considered to be potential candidates to show high-temperature superconductivity [32,33].

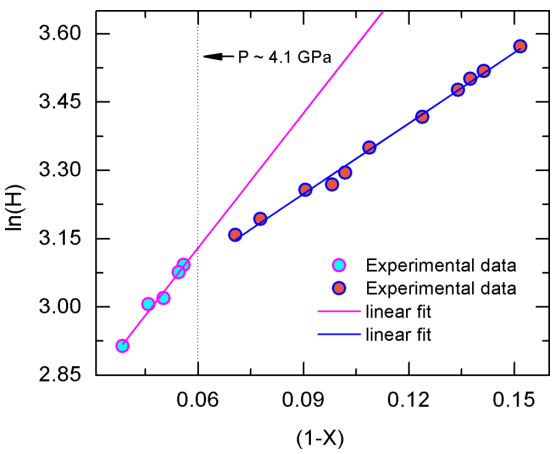

FIG. 14. Universal equation of state, i.e., lnH vs $(1 - X)$, where $H = [PX^2/3(1 - X)]$ and $X = (V/V_o)^{1/3}$ for CsI_3 in the trigonal phase. The dotted line denotes the electronic transition point.

V. SUMMARY AND CONCLUSION

In summary, the ambient temperature high-pressure behavior of CsI_3 investigated using three complementary high-pressure techniques, *viz.*, ADXRD, Raman, and electrical resistance measurement, indicate three-phase transitions up to 29 GPa. The onset of the ambient orthorhombic-to-trigonal structural phase transition is found to occur above 1.3 GPa and is associated with a volume discontinuity of 4.5%. The coexistence of the orthorhombic and trigonal phase is observed up to 10 GPa. The stability region of the trigonal phase is found to be up to 22.6 GPa, above which the trigonal phase transforms to a cubic phase which remains stable until the maximum pressure of 29 GPa achieved in this study. The present study has thus revealed a three-phase structural sequence in alkali trihalides, *viz.,* orthorhombic (SG: *Pnma*) to trigonal (SG:*P*-3*c*1) to finally cubic phase (SG : *Pm*-3*n*). In addition to the structural phase transitions, an electronic transition has also been observed around 4.0 GPa. The results of the present investigation thus throw light on the structural transition sequence of alkali polyhalides as a whole and provide useful inputs in understanding and standardizing the pressure effects on the alkali trihalide systems. The observation of a trigonal phase intermediate between the orthorhombic and the cubic phase in our study as against the theoretical prediction of a direct orthorhombic-to-cubic phase transition at 7.8 GPa will encourage further improvements in computational models for detailed theoretical investigation of alkali polyhalides.

ACKNOWLEDGMENTS

ADXRD measurements were carried out under Proposal No. 20155226 at the Elettra Synchrotron Source, Trieste, Italy. N.N.P. and M.S. gratefully acknowledge Dr. S. Karmakar, Dr. A. Lausi, Dr. B. Joseph, and Dr. P. Lotti for help in x-ray measurements at Elettra and the Indian DST for local hospitality and air travel support.

[1] S. Wei, C. Zhu, Q. Li, Y. Zhou, Q. Li, and Y. Ma, Phys. Chem. Chem. Phys. **16**, 17924 (2014).
[2] T. L. Huang and A. L. Ruoff, Phys. Rev. B **29**, 1112 (1984).
[3] Y. Xu, J. S. Tse, A. R. Oganov, T. Cui, H. Wang, Y. Ma, and G. Zou, Phys. Rev B **79**, 144110 (2009).
[4] H. K. Mao, Y. Wu, R. J. Hemley, L. C. Chen, J. F. Shu, L. W. Finger, and D. E. Cox, Phys. Rev. Lett. **64**, 1749 (1990).
[5] X. Chen and Y. Ma, Europhys. Lett. **100**, 26005 (2012).
[6] D. L. Decker, J. Appl. Phys. **42**, 3239 (1971).
[7] W. Zhang, A. R. Oganov, A. F. Goncharov, Q. Zhu, S. E. Boulfelfel, A. O. Lyakhov, E. Stavrou, M. Somayazulu, V. B. Prakapenka, and Z. Konopkova, Science **342**, 1502 (2013).
[8] W. Zhang, A. R. Oganov, Q. Zhu, S. S. Lobanov, E. Stavrou, and A. F. Goncharov, Sci. Rep. **6**, 26265 (2016).
[9] N. N. Patel, Ashok K. Verma, A. K. Mishra, M. Sunder, and S. M. Sharma, Phys. Chem. Chem. Phys. **19**, 7996 (2017).
[10] G. L. Clark, Proc. Natl. Acad. Sci. USA **9**, 117 (1923).
[11] S. Wei, J. Wang, S. Deng, S. Zhang, and Q. Li, Sci. Rep. **5**, 14393 (2015).
[12] G. L. Breneman and R. D. Willett, Acta Crystallogr., Sect. B: Struct. Sci., Cryst. Eng. Mater. **25**, 1073 (1969).
[13] C. L. Rose and S. Mooney, Acta Cryst. **12**, 187 (1959).
[14] J. C. Slater, Acta Cryst. **12**, 197 (1959).
[15] J. I. Musher, Angew. Chem. Int. Ed. **8**, 54 (1969).
[16] G. N. Lewis, J. Am. Chem. Soc. **38**, 762 (1916).
[17] G. C. Pimentel, J. Chem. Phys. **19**, 446 (1951).
[18] R. M. Bozorth and L. Pauling, J. Am. Chem. Soc. **47**, 1561 (1925).
[19] H. A. Tasman and K. H. Boswijk, Acta Cryst. **8**, 59 (1955).
[20] K. Odagi, H. Nakayama, and K. Ishii, Bull. Chem. Soc. Jpn. **63**, 3277 (1990).
[21] A. Lausi, M. Polentarutti, S. Onesti, J. R. Plaisier, E. Busetto, G. Bais, L. Barba, A. Cassetta, G. Campi, D. Lamba, A. Pifferi, S. C. Mande, D. D. Sarma, S. M. Sharma, and G. Paolucci, Eur. Phys. J. Plus **130**, 43 (2015).
[22] A. P. Hammersley, S. O. Svensson, M. Hanfland, A. N. Fitch, and D. Hausermann, High Pressure Res. **14**, 235 (1996).
[23] A. C. Larson and R. B. Von Dreele, Los Alamos National Laboratory Report LAUR 86-748, 1994.
[24] P. W Bridgmann, J. Appl. Phys. **12**, 461 (1941).
[25] R. Shirley, *The Crysfire 2002 System for Automatic Powder Indexing: User's Manual* (Lattice Press, Guildford, UK, 2002).
[26] P. E.Werner, L. Eriksson, and M. Westdahl, J. Appl. Cryst. **18**, 367 (1985).
[27] J. Laugier and B. Bochu, *CHEKCELL Graphical Indexing and Spacegroup Assignment Helper Tool* (Lattice Press, Guildford, UK, 2002).
[28] F. Birch, J. Geophys. Res. **83**, 1257 (1978).
[29] See Supplemental Material at http://link.aps.org/supplemental/10.1103/PhysRevB.96.174114 for Rietveld refined ADXRD patterns.
[30] J. H. Rose, J. R. Smith, F. Guinea, and J. Ferrante, Phys. Rev. B **29**, 2963 (1984).
[31] S. K. Sikka, Phys. Rev. B **38**, 8463 (1988).
[32] P. Baettig and E. Zurek, Phys. Rev. Lett. **106**, 237002 (2011).
[33] J. Hooper and E. Zurek, J. Phys. Chem. C **116**, 13322 (2012).